X-ray Scattering Studies of Maquette Peptide Monolayers. 1. Reflectivity and Grazing Incidence Diffraction at the Air/Water Interface

Joseph Strzalka,*,† Xiaoxi Chen,‡ Christopher C. Moser,‡ P. Leslie Dutton,‡ Benjamin M. Ocko,§ and J. Kent Blasie†

Department of Chemistry and Department of Biochemistry and Biophysics, University of Pennsylvania, Philadelphia, Pennsylvania 19104, and Department of Physics, Brookhaven National Laboratory, Upton, New York 11973

Received February 24, 2000. In Final Form: July 21, 2000

We present isotherm and X-ray reflectivity (XR) measurements from Langmuir monolayers of a *de novo* synthetic di-α-helical peptide, consisting of two identical 31-residue, mostly α-helical peptide units joined by a disulfide bond at their amino-termini. Fitting the XR data to slab models shows that the dihelices lie in the plane of the interface at low pressures. The monolayers were insufficiently stable for study at high pressures, but Langmuir films based on a derivative of the peptide alkylated at its amino termini permitted investigations over a larger range of pressures. We observed an orientational transition, in which the α-helices begin by lying in the plane of the interface at low surface pressures and orient themselves approximately normal to the interface at high pressures. We draw the same conclusions from the XR data when we analyze it using box refinement, an iterative, model-independent method for recovering structure from XR data. Mixtures of these palmitoylated peptides with a fatty acid (palmitic acid) or a phospholipid (DLPE) behaved similarly. None of the systems produced peaks in the grazing incidence diffraction signal indicative of long-range ordering of the upright α-helices. Off-specular in-plane scattering measurements based on the difference signal between the peptide/DLPE mixture and pure DLPE suggest that the peptide achieves only liquidlike order within the plane. We discuss the implications and prospects for future work on designed peptide monolayers incorporating prosthetic groups that could be used to study electron transfer in proteins and provide a basis for biomolecular electronics applications.

Introduction

Nature uses a variety of proteins with special prosthetic groups to control processes such as electron transfer in photosynthesis and oxidative phosphorylation. The complexity of the proteins involved defies easy investigations of the relationship between their structure and function. Recently, smaller *de novo* synthetic peptides have been developed whose composition and properties can be readily explored and modified as a stepping stone toward understanding naturally occurring proteins.[1] These so-called "maquettes" provide model systems for testing theories of electron transfer in proteins. A family of maquettes based upon a four-helix bundle motif has been designed and synthesized. The general synthetic strategy utilizes a 31-residue peptide whose primary sequence is designed to be mostly an amphipathic α-helix except for three glycine and one cysteine residues at the amino terminus. The side-chain sulfhydryl group of the N-terminal cysteines dimerizes via a disulfide linkage to form a dihelical unit which then self-assembles in isotropic aqueous solution to form a four-helix bundle. Histidine residues at apposed positions in each helix of the dihelical unit can then be utilized for bis-histidyl ligation of metalloporphyrin prosthetic groups at one or more sites in the primary sequence. Heme groups bound to these sites have been demonstrated to have spectral and electrochemical properties closely resembling those of redox proteins found in nature. In order for meaningful data to be extracted from electrochemical measurements, experimenters need to know the structure of the molecule so that electron-transfer rates can be related to the distance and medium through which the transfer occurs. X-ray and neutron studies performed on thin-film samples can provide this key information.

A thin, monomolecular film of protein molecules covering a planar electrode comprises the simplest and most effective geometry for electron transfer studies and also constitutes an appropriate specimen for reflectivity measurements, making correlated structural/functional studies possible. Once the electron-transfer properties of maquettes and the means to design desired properties are sufficiently understood, this geometry offers a basis for biomolecular electronics applications.

We set as our goal the creation of dense, well-ordered films of maquette peptides on solid supports. We concentrated on Langmuir−Blodgett techniques for achieving such a film since control of the surface pressure of the precursor Langmuir monolayer affords us a macroscopic means of varying such microscopic properties as the density and orientation of the molecules in the film. The anisotropic nature of the interface can confine suitably designed amphiphilic molecules to the plane of the interface and orient them vectorially. This may in turn may provide a suitable environment for further organization, such as two-dimensional crystallization or the directed incorporation of prosthetic groups to particular binding sites. Due to advances in synchrotron X-ray scattering techniques, we were able to study directly the

* To whom correspondence may be addressed: Department of Chemistry, Box 141, University of Pennsylvania, Philadelphia, PA 19104-6323; strzalka@jkb2.chem.upenn.edu.

† Department of Chemistry, University of Pennsylvania.

‡ Department of Biochemistry and Biophysics, University of Pennsylvania.

§ Department of Physics, Brookhaven National Laboratory.

(1) Robertson, D. E.; Farid, R. S.; Moser, C. C.; Urbauer, J. L.; Mulholland, S. E.; Pidikiti, R.; Lear, J. D.; Wand, A. J.; DeGrado, W. D.; Dutton, P. L. *Nature* **1994**, *368*, 425−431.

10.1021/la000264z CCC: $19.00
Published on Web 12/01/2000

Langmuir films formed from two different maquettes. Related X-ray scattering studies of the resulting Langmuir−Blodgett monolayers will be reported separately.[2]

Methods and Materials

The Spreading Solutions. We used two different peptides in these investigations. The prototype 4-α-helix-bundle maquette peptide is denoted H10H24,[1] based on the histidine residues at sequence positions 10 and 24 employed for binding metalloporphyrin prosthetic groups via axial ligation, and has the amino acid sequence:

CGGGE LWKLH EELLK KFEEL LKLHE ERLKK L

We synthesized a more amphiphilic palmitoylated peptide derivative[3] with the amino acid sequence:

$CH_3 (CH_2)_{14}CO-$
CGGGE IWKLH EEFLK KFEEL LKLHE ERLKK L

In solution, the apo-form of the precursor unpalmitoylated peptide has a more stable conformation, as determined by NMR.[4,5] The peptide was originally referred to as H10H24(L6→I,L13→F) to emphasize that the sequence comes from H10H24, but with two substitutions. In this paper, we will refer to the precursor as BB and the palmitoylated derivative as BBC16, short names in common use in the lab.

We synthesized the peptides by implementing solid-phase synthesis with Fmoc chemistry in a MilliGen 9050 machine. The last step of the synthesis, palmitoylation of the peptide, is also accomplished while the peptide is still bound to the resin. We purify the 31-mer peptides via reverse-phase high-performance liquid chromatography (HPLC), lyophilize them, and then resolubilize them in a basic buffer solution to promote the formation of disulfide bonds between the N-terminal cysteine residues, thereby forming dihelical units composed of 62 residues. More details of the peptide preparation are given elsewhere.[3] The dimers are lyophilized and stored in a freezer. We prepare peptide spreading solutions as necessary by resolubilizing the peptide in 50 mM TRIS buffer (Sigma) with 100 mM NaCl. The peptide solutions remain usable when they are stored in a refrigerator. Sedimentation studies and size-exclusion chromotography establish that H10H24 and BB form four-helix bundles in solution. But size exclusion chromotography shows that BBC16, unlike its unpalmitoylated precursor, forms aggregates larger than four α-helices in solution, presumably due to the alkyl chain interactions.

1,2-Dilauroyl-*sn*-glycero-3-phosphoethanolamine (dilauroyl-phosphatidylethanolamine, DLPE) was purchased in a 10 mg/mL solution in chloroform from Avanti Polar-Lipids (Alabaster, AL) and diluted to 1 mg/mL by addition of HPLC grade chloroform.

The Liquid Surface Spectrometer. We performed all X-ray scattering experiments at beamline X22B of the National Synchrotron Light Source (Brookhaven National Laboratory, Upton, NY) on a liquid surface spectrometer that has been described in detail elsewhere.[6,7] In brief, the spectrometer consists of a two-circle stage mounted on the 2θ-arm of a four-circle diffractometer and allows X-rays to strike the sample at a range of incident angles, α, measured with respect to the liquid surface, while keeping it level. To do this, it lowers the sample on an elevator stage and bends the beam down to the sample using a Ge crystal mounted in the four-circle diffractometer. The detector, a scintillation counter, is mounted on the 2θ-arm of the sample two-circle stage and is positioned to accept X-rays scattering from the surface at an angle β with respect to the liquid surface. For reflectivity measurements, we keep the spectrometer in the reflectivity condition, $\alpha = \beta$, so as to collect the photons scattered with momentum transfer perpendicular to the liquid surface ($q_z = (4\pi \sin \alpha)/\lambda$). At each point q_z, we collect data with the detector in the plane of the reflection ($2\theta_{xy} = 0°$) for time t, and the background with the detector on either side of the plane ($2\theta_{xy} = \pm 0.3°$) for time $t/2$, and subtract the latter from the former. For grazing incidence diffraction (GID) over $2\theta_{xy}$, we used evacuated collimating Soller slits and set the incident angle to $\alpha = 0.12°$ ($q_z = 0.017$ Å^{-1}), below the critical angle of water ($\alpha = 0.153°$, $q_z = 0.0217$ Å^{-1}). Different measurements used two different detectors: the scintillation detector with a vertical aperture before it defining the acceptance and vertical resolution, or a position-sensitive detector (Braun) aligned parallel to the q_z-direction that could be read out pixel-by-pixel or in an intergrating mode. Most GID measurements were performed with Soller slits also aligned along the q_z-direction to improve the horizontal resolution. Note that for GID and Bragg rod (q_z-resolved GID) scans, α remains fixed, so that unlike the reflectivity condition, $\beta \neq \alpha$, and $q_z = (2\pi/\lambda) \sin(\alpha + \beta)$.

The Langmuir Trough and Monolayer Deposition. We deposit the monolayer in a custom-built Langmuir trough with a working area 26 × 11.6 cm and a Wilhelmy plate surface pressure transducer (Riegler & Kirstein, Germany). It is mounted on a vibration isolation stage on top of the sample stage. A Si block in the subphase helps further damp out oscillations of the free surface. The trough is enclosed in an aluminum box filled with moist He. A Kapton window permits the X-rays to enter and exit. Water from a thermostated bath circulates through a copper block in thermal contact with the bottom of the trough and maintains the subphase at constant pressure, usually 16 °C. The subphase typically consisted of a 1 mM TRIS buffer (SIGMA, St. Louis, MO), pH 7.8, prepared with MilliQ water (Millipore Corp., Bedford, MA).

As both the peptides are soluble in water to different extents, depositing them at the air/water interface requires great care. The spreading solution is similar in composition to the subphase: MilliQ water buffered at pH 8 by the addition of 50 mM TRIS, with 100 mM NaCl, and typically a 100 μM concentration of 31-mer α-helical units. To promote formation of a monolayer, we use a microliter pipet to deposit the solution dropwise at the thin film of water provided by the meniscus that forms over a glass capillary penetrating the air/water interface at an oblique angle. We typically deposited a sufficient volume of the peptide solution, about 150 μL, to obtain a small but noticeable increase in surface pressure (~0.5 mN/m). The dropwise deposition itself requires about 15 min, and then we typically waited another 20 min before compression. During this time, the surface pressure continues to increase slightly, to about 0.7 mN/m. For mixed monolayers with DLPE, we deposited the chloroform-based lipid

(2) Strzalka, J.; Chen, X.; Moser, C. C.; Dutton, P. L.; Bean, J.; Blasie, J. K. Submitted for publication in *Langmuir*.

(3) Chen, X.; Moser, C. M.; Pilloud, D. L.; Dutton, P. L. *J. Phys. Chem. B* **1998**, *102*, 6425−6432.

(4) Gibney, B. R.; Rabanal, F.; Skalicky, J. J.; Wand, A. J.; Dutton, P. L. *J. Am. Chem. Soc.* **1997**, *119*, 2323−2324.

(5) Skalicky, J. J.; Bieber, R. J.; Gibney, B. R.; Rabanal, F.; Dutton, P. L.; Wand, A. J. *J. Biol. NMR* **1998**, *11*, 227−228.

(6) Weiss, A. H.; Deutsch, M.; Braslau, A.; Ocko, B. M.; Pershan, P. S. *Rev. Sci. Instrum.* **1986**, *57*, 2554−2559.

(7) Braslau, A.; Pershan, P. S.; Swislow, G.; Ocko, B. M.; Als-Nielsen, J. *Phys. Rev. A* **1988**, *38*, 2457−2470.

solution directly to the surface first, waited a few minutes for the chloroform to evaporate, and then deposited the aqueous peptide solution over a capillary. Spreading the same amount of peptide in the presence of a lipid would cause a greater initial pressure, between 3 and 6 mN/m. We compressed at a rate of 10−20 mm/min (30−60 Å^2/α-helix/min) until the desired surface pressure was achieved and then maintained constant pressure during the X-ray measurements.

Collecting data at the highest surface pressures (>30 mN/m) required an extra complication in the deposition process, as the maximum ratio of the trough's fully expanded to fully compressed area was about 3. At the start of the deposition, we laid a Teflon block with a half-inch-square cross section across the trough directly in front of the barrier. Then we deposited the pure peptide or mixed peptide/lipid monolayer as usual in the remaining area. We compressed the film through almost the entire range with the Teflon block pushed along in front of the barrier, preventing the barrier itself from making contact with the film. This would result in a surface pressure of about 30 mN/m which would begin to relax once the barrier motion stopped, approaching a limiting value of about 20 mN/m after about 20 min. During this time, we moved the barrier back to its starting position. The Teflon block remained in place, keeping the monolayer in its compressed state. In the fraction of the area of the trough now available between the barrier and the Teflon block, we spread an amount of peptide and lipid proportional to the amount that was initially spread on the entire trough. After waiting the usual time before compression of a newly deposited peptide film, we carefully removed the Teflon block, waited an additional 15−20 min, and compressed the resultant film. By means of this two-stage deposition process, we could increase the compression ratio to about 5, achieve surface pressures over 40 mN/m, and still keep the pressure constant during X-ray measurements.

Data Reduction and Analysis. Data reduction and analysis via slab model refinement were performed on Silicon Graphics workstations using the program C-Plot (CSS). The nonlinear least-squares fitting package of the program implements the Marquardt algorithm[8] and permits data to be fit with user-defined functions incorporating slab models as briefly described by Tidswell et al.[9] and reviewed by Als-Nielsen and co-workers.[10] We confirmed the results obtained from fitting the data by applying box refinement, an iterative approach to recovering electron density distributions from reflectivity data (see the Appendix for details). This method provides a solution to the phase problem and is applied here for the first time to normalized reflectivity data.

Results and Discussion for Pure Peptide Monolayers

Experimental Results. Despite some minor differences in their amino acid sequences, we may consider BBC16 as the palmitoylated derivative of the peptide H10H24, the prototype of a family of the four-helix bundle maquette peptides. Both peptides form a covalently bonded dihelical unit with similar metalloporphyrin binding properties. However, sedimentation studies show that the dihelices of H10H24 further associate into four-helix bundles in isotropic aqueous solution while BBC16, due to the hydrocarbon chain, has a substantially higher aggregation state. The isotherms recorded for pure monolayers of these peptides appear in Figure 1 and share common elements, notably a plateau at about 30 mN/m, but at small areas, below 200 Å^2/α-helix, the isotherms for the two peptides differ strongly. Pressure begins to increase only gradually for the H10H24 monolayer as its area is decreased, while for BBC16 it increases sharply. As the diameter of an α-helix is about 10 Å, and its pitch is about 1.5 Å/residue, a 31-residue α-helix lying on its side should cover roughly 450 Å^2, while its cross-sectional area should be about 100 Å^2. Comparing these numbers with the isotherms suggests that the peptide is oriented with its long axis parallel to the interface at low pressures, until it becomes close packed, when the molecular axis changes its orientation to be normal to the interface, and pressure increases again as the upright helices approach close packing. For BBC16, this would place the α-helices in the subphase while the hydrocarbon chain remains in the air. We applied X-ray reflectivity to observe this behavior directly.

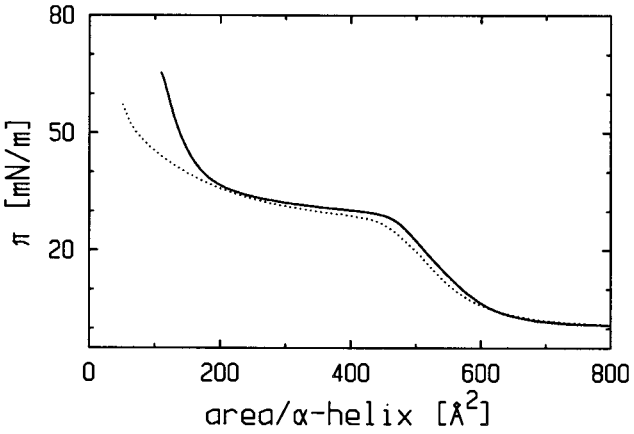

Figure 1. The isotherms for monolayers of the peptide H10H24 (dotted) and the lipopeptide BBC16 (solid) show that palmitoylation of the α-helices creates a second region with rapidly increasing pressure beyond the plateau region. Both monolayers deposited on 1 mM phosphate buffer, pH 8.0 at 10°.

Figure 2 shows the normalized reflectivity from pure monolayers of BBC16, one at a pressure below the plateau in the isotherm and two at pressures above the plateau. The low-pressure data consist of a single, broad maximum, while the data recorded at pressures above the plateau possess several maxima with an amplitude that decays as q_z increases.

Considering the monolayer as a medium of constant density L Å thick, the so-called single slab model, reflectivity theory predicts a simple cosine dependence ($\cos(qL)$) to the oscillations in the normalized reflectivity.[9,10] Accordingly, such a decrease in the period of the oscillations in q-space must correspond to a dramatic increase in the thickness of the monolayer in real space. Such a model does fit the data adequately, with the thickness of the slab changing from 10 Å to nearly 58 Å. While two-slab models for the data at high pressure are more consistent with the separate peptide and hydrocarbon moieties of BBC16, they do not improve the fits substantially and they introduce somewhat larger uncertainties in the parameters determined. The real space electron density distributions, or profile structures, computed from the fit parameters appear in Figure 3. The two-slab and one-slab models give identical profiles. In the low-pressure case, when the interfacial roughness is

(8) Bevington, P. R.; Robinson, D. K. *Data Reduction and Error Analysis for the Physical Sciences*, 2nd ed.; McGraw-Hill, Inc.: New York, 1992.

(9) Tidswell, I. M.; Ocko, B. M.; Pershan, P. S.; Wasserman, S. R.; Whitesides, G. M.; Axe, J. D. *Phys. Rev. B* **1990**, *41*, 1111−1128.

(10) Als-Nielsen, J.; Jacquemain, D.; Kjaer, K.; Leveiller, F.; Lahav, M.; Leiserowitz, L. *Phys. Rep.* **1994**, *246*, 251−313.

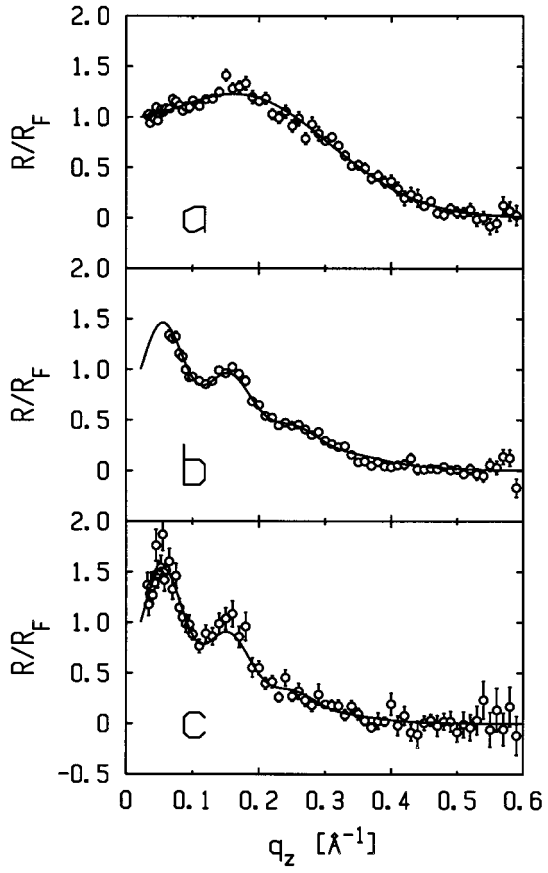

Figure 2. Normalized reflectivity data and fits obtained from one-slab models (solid curves) for pure BBC16 monolayers at different surface pressures: $\pi = 22$, 33, and 40 mN/m in a, b, and c, respectively.

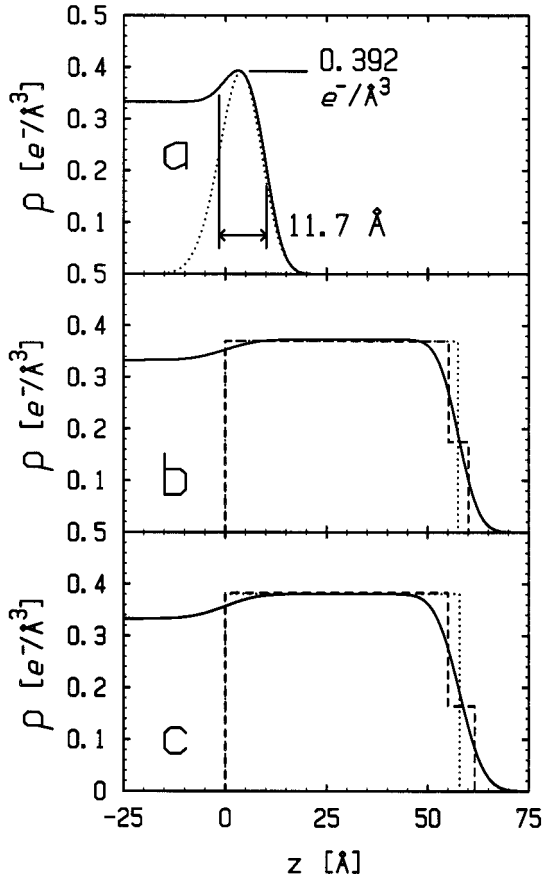

Figure 3. Electron density profile structures for pure BBC16 monolayers at different surface pressures: $\pi = 22$, 33, and 40 mN/m in a, b, and c, respectively. The profiles, constructed from the parameters in Table 1, correspond to the fits shown in Figure 2. For the low-pressure case, a, the interfacial roughness makes the narrow slab model appear broader and less dense than the fit parameters might otherwise suggest. For comparison, the dotted line in part a shows the projection from the model atomic coordinates for a single α-helix of H10H24. In parts b and c, the dotted and dashed lines show the one- and two-slab models that best fit the data with the interfacial roughnesses neglected. In both parts b and c, the models result in the same electron density distribution when the effect of interfacial roughness is included (the solid curve).

comparable to the thickness of the slab, the profile structure is actually somewhat broader and less dense than the fit parameters might otherwise suggest.

Monolayers of H10H24 were insufficiently stable for us to obtain reflectivity data at pressures above the plateau in the isotherm. Reflectivity data collected from several monolayers investigated at pressures below the plateau were similar to that for BBC16 at low pressures, with a single broad maximum (data not shown). As was also done with BBC16, we constrained the interfacial roughness parameters, $\sigma \geq 3.2$ Å, the value typically observed from a clean air/water interface. Coupling between the parameters causes a range of parameters to give nearly identical fits to the data. Since the resulting profile structures differ only very slightly, the constraint amounts to choosing the parameter set with a physically meaningful roughness from a set of nearly equivalent mathematical solutions.

In both systems, we scanned for GID in the region $1 < 2\theta_{xy} < 10°$ (d-spacing between 8.8 and 88 Å) in order to seek evidence of ordering of the α-helices within the plane, but we did not observe any peaks. We did not scan the region around $2\theta_{xy} = 20°$ where evidence of hydrocarbon chain packing might be found, because we expected them to be highly disordered, as they are constrained to exist at large excess area per chain.

Discussion. The data clearly demonstrate that the BBC16 peptide undergoes an orientational transition within the monolayer, in which its long axis changes from being parallel to the plane of the air/water interface at low pressures to being normal to the interface at high pressures. To show this, we consider simple calculations based upon model atomic coordinates of H10H24.[1]

If we take one α-helix of the model and compute the projection of its electron density distribution onto the coordinate along a diameter of the helix, the result agrees well with the profile structures obtained from the one-slab fits to the reflectivity data collected from monolayers of BBC16 and H10H24 at low pressures, as shown in Figure 3a. This indicates that upon deposition at the air/water interface, the peptide exists at the interface as dihelical units lying with the long axis of the helices lying in the plane of the interface. By design, the hydrophilic residues occur on one side of the helix while hydrophobic residues and the histidines for prosthetic group ligation occur on the other, rendering it amphipathic. In solution, four-helix bundles form in order to minimize the peptide's energy by burying all the hydrophobic residues in the core of the bundle, but four-helix bundles in the monolayer would result in a profile thicker by a factor of 2, inconsistent with the experimental result. Presumably, the asymmetric environment of the interface allows the peptide to minimize its energy by exposing its hydrophobic face to the air and its hydrophilic face to the subphase.

Table 1. Fit Parameters for the Reflectivity Data Collected on Pure Monolayers of BBC16 as Shown in Figure 2[a]

π (mN/m)	A/α-helix (Å^2)	L_1 (Å)	ρ_1 (e$^-$/Å^3)	σ_0 (Å)	σ_1 (Å)	L_2 (Å)	ρ_2 (e$^-$/Å^3)	σ_2 (Å)
22	460	10.0	0.420	3.5[b]	3.5			
33	160	57.5	0.370	6.2	4.1			
		55.2	0.370	6.1	3.2	4.9	0.175	3.2
40	135	57.9	0.381	6.6	4.8			
		55.0	0.383	6.4	3.2	6.6	0.164	3.2

[a] The electron density profile structures constructed from these parameters appear in Figure 3. High-pressure data were fit with both one-slab and two-slab models. The parameter σ_0 gives the subphase/slab 1 interfacial roughness; σ_1 the slab 1/helium or the slab 1/slab 2 roughness; and σ_2 the slab 2/helium roughness. Area/α-helix values are taken from the isotherm shown in Figure 4 (the dotted curve). [b] Constraint $\sigma \geq 3.5$ Å applied for this fit.

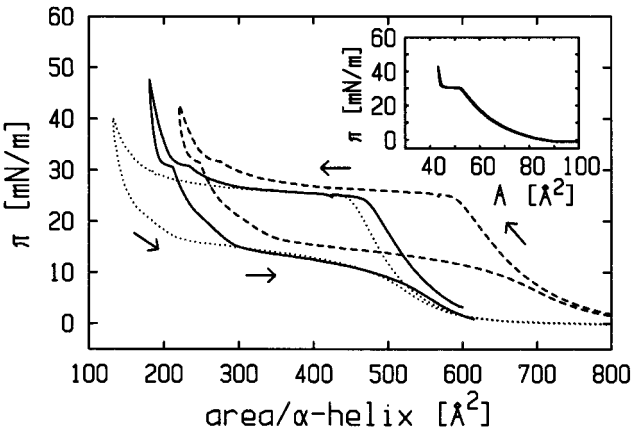

Figure 4. Isotherms of 2:1 DLPE/BBC16 mixtures at 16 °C on 1 mM TRIS buffer, pH 7.8, with arrows indicating the compression and expansion parts of the cycle. The dashed line corresponds to a monolayer deposited with $\pi_0 = 0$ mN/m while the solid line corresponds to a monolayer deposited with finite initial pressure. Note the difference in final area/α-helix. For comparison, a pure BBC16 monolayer is also shown (dotted line). The inset shows the isotherm for pure DLPE, which exhibits almost identical curves for compression and expansion. Note that the kink in the isotherm for the mixture occurs at the same pressure where the plateau occurs in pure DLPE.

Similarly, the high-pressure data from BBC16 also agree well with our expectations for α-helices oriented normal to the air/water interface. Combining the fit parameters (Table 1) with the area/α-helix from the isotherm for pure BBC16 of Figure 4 (dotted curve), collected under the same conditions as the reflectivity data, we compute the number of electrons contained within a "unit cell" containing one α-helix. One α-helix has 1733 electrons (e$^-$), while the palmitoyl chain contributes 95 e$^-$, so excess e$^-$ must be due to water within the monolayer, consistent with the monolayer e$^-$ density being intermediate between that of water, $\rho_{water} = 0.333$ e$^-$/Å^3 and that of densely packed protein, $\rho_{protein} = 0.420$ e$^-$/Å^3. This implies that there are 158 water molecules/α-helix at 33 mN/m and 115 at 40 mN/m. Since the volume of a water molecule is 29.9 Å^3, this corresponds to a change in the volume of the unit cell of 1246 Å^3, within 10% of the observed change in volume, 1384 Å^3. We may also consider the ratio of the number of e$^-$ in the α-helix to the total number of e$^-$ in the one-slab fits, $f = N_{alpha}/N_{total}$. The density obtained from the fit agrees well with that computed from $f\rho_{protein} + (1 - f)\rho_{water}$ (namely, for $\pi = 33$ mN/m, 0.377 e$^-$/Å^3 vs 0.370 from the fit and for $\pi = 40$ mN/m, 0.384 e$^-$/Å^3 vs 0.381).

Comparing the observed thickness of the monolayer at high pressures to our expectations is complicated by the presence of the sparsely populated hydrocarbon layer. If we assume that all 31 residues of the peptide pack α-helically, than we expect a length of 31 × 1.5 Å/residue = 46.5 Å. The palmitoyl chain has an all trans length of (14 + 9/8) × 1.265 Å = 19.13 Å, excluding the carboxyl group peptide bonded to the cysteine residue. As the chain is covalently bound to an α-helix and so constrained to occupy about 5 times the area that it would occupy when close packed, it is likely that its average chain configuration would be highly disordered compared to an all trans configuration. The length of the one-slab model is shorter than the sum of the expected peptide length and the extended all trans hydrocarbon chain length, as is the total length of the two-slab model. The two-slab model suggests that the profile structure of the BBC16 monolayers can be decomposed into a dense peptide slab about 55 Å thick and a less dense hydrocarbon slab 5−7 Å thick. If this is in fact the case, then the peptide slab is still thicker than expected. However, the interface between the peptide and the hydrocarbon chains is not very well defined here, and as noted above, the precision of the data do not really merit fitting with two-slab models, although they do provide physically reasonable results.

The pressure-dependent change in orientation undergone by BBC16 is clearly established by the experimental data. H10H24 need not undergo a similar transition in its orientation at high pressures, because without a distinct hydrophobic moiety to anchor it to the interface, this peptide can form four-helix bundles thereby losing its amphiphilicity and making the monolayer unstable at high pressures. Modification of the prototype maquette peptide through palmitoylation succeeded in creating a monolayer stable enough for us to achieve one of our aims, control over the microscopic orientation of the peptide via the surface pressure applied to the film macroscopically. On the other hand, the hydrocarbon part of the monolayer is only sparsely packed and disordered because the palmitoyl moiety is so much smaller in cross section than the α-helix to which it is bonded. Improving the ordering of the chains should sharpen the interfaces of the monolayer and extend the reflectivity to higher q_z, allowing characterization of the peptide at higher resolution. Two approaches might effect the change: a synthetic route and an engineering route. Synthetically, one might try to modify the peptide itself, perhaps by coupling the peptide to a larger hydrophobic group more commensurate with the cross-sectional area of an α-helix. From an engineering perspective, one might try to modify the monolayer as a whole by adding surfactants to enhance the stability and ordering of the monolayer. Our subsequent experiments followed the latter approach.

Results and Discussion for BBC16/DLPE Mixtures

To engineer a better monolayer, we tried two different surfactants, the fatty acid palmitic acid and the phospholipid DLPE. As the fatty acid did not significantly improve the ordering or the stability of the monolayers,[11] we will not report the results here. We chose DLPE because

(11) Strzalka, J. X-ray Scattering Studies of Maquette Peptide Monolayers. Thesis, University of Pennsylvania, 2000.

this short chain length (C_{12}) phospholipid undergoes the fluid to gel phase transition at high surface pressures and so will remain fluid as the peptide changes its orientation. We expected this to improve the chances for crystallizing the peptide. The greater stability of the pure DLPE and DLPE/BBC16 mixed monolayers relative to palmitic acid monolayers also allowed two improvements to our inplane scattering methodology: (1) we could integrate for longer periods of time to increase our counting statistics; (2) this in turn made it possible to employ difference techniques to isolate the scattering signal due to the peptide moiety.

Isotherms. Monolayers of pure DLPE do not build up any pressure until they are compressed beyond molecular areas of about 90 Å^2 (inset, Figure 4). The pressure increases until it reaches a sharp kink that introduces a plateau at π_c and begins to increase again as the limiting molecular area of 40 Å^2 is approached. The kink marks the onset of a phase transition from the low-pressure purely fluid phase to an ordered gel phase,[12] as is typical of all phospholipid isotherms.[13] The plateau represents a coexistence between the fluid phase and gel phase and is the first place in the isotherm in which peaks become observable in GID scans.[12] Unlike the peptide monolayers, monolayers of DLPE have reversible isotherms.

We spread mixed monolayers of BBC16 and DLPE in a ratio of two DLPE molecules for each α-helix. Every α-helix had one covalently bound palmitoyl chain and four additional hydrocarbon chains, two pairs of lauroyl chains, each pair bound to the glycerol backbone of the phospholipid molecule. We based this strategy on the approximately 5:1 ratio between the minimal cross-sectional areas of hydrocarbon chains and α-helices. The isotherms of the mixed monolayers are shaped similar to that of the pure lipopeptide, except for the presence of a kink at the same pressure as the phase transition in the pure DLPE monolayers (Figure 4). The range of the area/α-helix that the isotherm spans, however, varies depending upon the deposition conditions. When the monolayer is spread at excess area, so that there is practically no initial surface pressure, the initial rise in pressure occurs at large area/α-helix (≈800 Å^2) and the limiting area reached is about 215 Å^2. When the monolayer is deposited so that the initial area/α-helix corresponds to an area where the pure lipopeptide monolayer already exhibits a finite pressure, a larger pressure is observed for the mixture before compression, between 3 and 5 mN/m. The pressure increases immediately and a final area/α-helix is reached that is intermediate between that of the pure lipopeptide and that of the mixture spread at excess area.

The isotherms of the mixed DLPE/BBC16 monolayers suggest that the lipid will not pack together with the lipopeptide in such a way as to promote ordering of the hydrocarbon tails of the lipopeptide. Judging from the area/α-helix at high pressures, we draw the conclusion that the lipid competes with the peptide for area at the interface. When the monolayer is deposited with effectively zero initial pressure, the lipid competes most effectively and the area/α-helix is about what we expect for the sum of the molecular area of one α-helix in the pure lipopeptide monolayer plus two DLPE molecules in a pure phospholipid monolayer at that pressure. When the monolayer is spread with finite initial pressure, the limiting area at high pressures is smaller than the sum of the limiting areas of the components, so it appears that some of the phospholipid does occupy the excess area over the helices of the peptide component. The isotherms do not give direct evidence of the degree of mixing of the two components. The lipid and the lipopeptide may be mixed locally or separated into single-component domains or some coexistence of both mixed and separated domains may occur. The decrease in the limiting specific area that occurs when the monolayer is deposited with finite initial pressure, though, implies that at least some mixing does occur. Judging from the value of the limiting specific area, about one-third to one-half of the phospholipid must occupy the excess area over the helices. Figure 5 shows a schematic representation of the molecular arrangements considered here. Although the most probable molecular arrangement (Figure 5d) is not the ideal case (Figure 5a), the enhancement of the monolayer stability that DLPE affords us made it worthy of inclusion in our synchrotron studies.

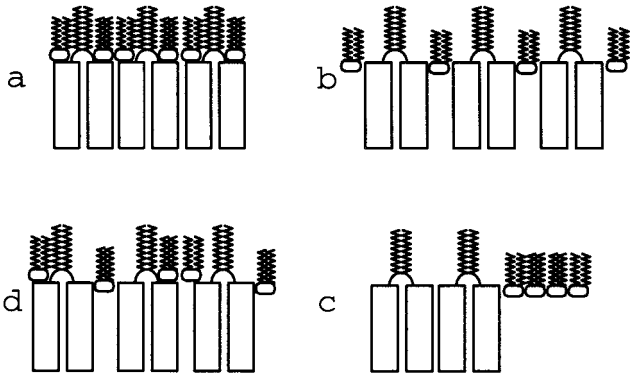

Figure 5. Cartoons of the possible interactions between BBC16 and DLPE at the air−water interface: (a) DLPE fills in excess area around the hydrocarbon chains of the lipopeptide; (b) DLPE mixes with the peptide but competes with it for area at the interface; (c) DLPE does not mix with the peptide; (d) some DLPE occupies the excess area around the lipopeptide's palmitoyl chains and some of it competes with the peptide for area at the interface. Cases b and c would be consistent with isotherms collected after deposition with zero initial pressure, while case d agrees with deposition at finite initial pressure.

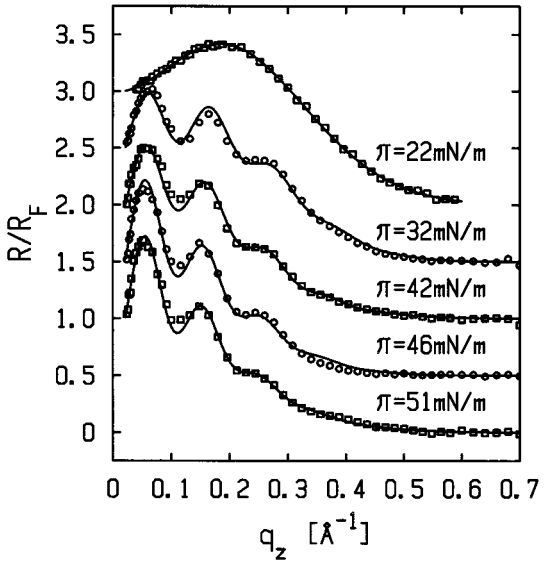

Figure 6. Normalized reflectivity data for DLPE/BBC16 2:1 monolayers and the slab-model fits to the data (solid curves). Data sets for different pressures have been offset for clarity.

Reflectivity. We collected reflectivity data on several mixed monolayers of DLPE and BBC16 at various surface pressures. One dataset at a pressure below the plateau in the isotherm consists of a single broad maximum (Figure 6, top curve), as was observed for the pure peptides at low

(12) Helm, C. A.; Tippmann-Krayer, P.; Möhwald, H.; Als-Nielsen, J.; Kjaer, K. *Biophys. J.* **1991**, *60*, 1457−1476.

(13) Helm, C. A.; Möhwald, H.; Kjaer, K. Als-Nielsen, J. *Biophys. J.* **1987**, *52*, 381−390.

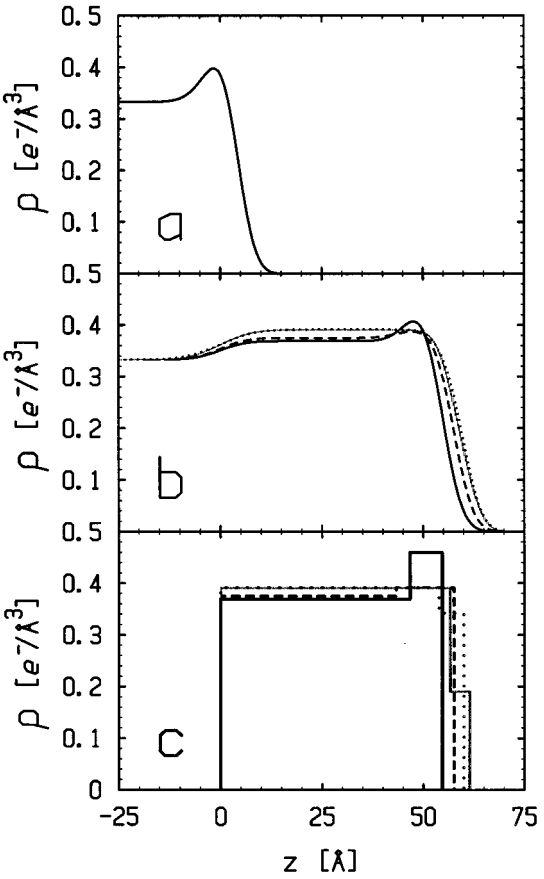

Figure 7. Electron density profile structures of DLPE/BBC16 2:1 monolayers constructed from the parameters given in Table 2 for the fits shown in Figure 6: (a) a one-slab model profile for $\pi = 22$ mN/m (below the plateau in the isotherm); (b) two-slab model profiles for various surface pressures above the plateau in the isotherm at 32 (solid curve), 42 (fine dashed curve), 46 (coarse dashed curve), and 51 mN/m (dotted); (c) the same profiles as in b—but with interfacial roughnesses neglected— show how the second slab puts electron density in the headgroup region at lower pressures and in the tail region for higher pressures.

pressure. We fit the dataset with a one-slab model, from which we construct an electron density profile structure that indicates that the helices are lying with their helix axes in the plane of the interface (Figure 7a). When the helices lie in the plane of the interface, they occupy the vast majority of the surface area, so that it is not surprising that the presence of DLPE cannot be discerned within the reflectivity data. The other datasets, collected at pressures above both the plateau in the isotherm of the mixed monolayer and above the kink at π_c in pure DLPE, possess three maxima with an overall shape and periodicity similar to what was seen for the pure lipopeptide at high pressures. As the surface pressure increases, the ratio of the amplitudes of the first and second maxima in the normalized reflectivity increases. The data were best fit by two-slab models in which the monolayer/subphase interface had a roughness different from that for the slab/slab interface and the monolayer/air interface.[14] These models are consistent with a perpendicular orientation of the

(14) As will be discussed below, inplane scattering experiments showed evidence of some phase separation between the components of the monolayer. However, modeling the data as a superposition between pure peptide and phospholipid domains did not result in reasonable fits. Considering how much the data from the mixture resembles that from the pure peptide, this outcome is not surprising and implies that the extent of phase separation must be very small.

Table 2. Fit Parameters for the Reflectivity Data Collected on Mixed Monolayers of DLPE and BBC16 in a Ratio of 2 DLPE Molecules for Each α-Helix of BBC16, as Shown in Figure 6[a]

π (mN/m)	L_1 (Å)	ρ_1 (e⁻/Å³)	σ_0 (Å)	σ_1 (Å)
22	4	0.600	5.1	3.6
32	46.7	0.369	5.0	3.9
42	43.3	0.374	5.2	3.8
46	55.7	0.391	6.2	3.2[b]
51	53.9	0.392	7.1	3.7
π (mN/m)	L_2 (Å)	ρ_2 (e⁻/Å³)	σ_2 (Å)	χ^2
32	8	0.460	σ_1	12.61
42	14.3	0.391	σ_1	10.13
46	4.9	0.190	σ_1	25.98
51	6.2	0.342	σ_1	11.65

[a] The corresponding electron density profile structures are shown in Figure 7. The roughness parameters for the subphase/slab 1, slab 1/slab 2, and slab 2/helium interfaces are given by σ_0, σ_1, and σ_2, respectively, except for the $\pi = 22$ mN/m case, which could be fit with a one-slab model in which σ_1 describes the slab/helium interface. [b] Constraint $\sigma \geq 3.2$ Å applied for this fit.

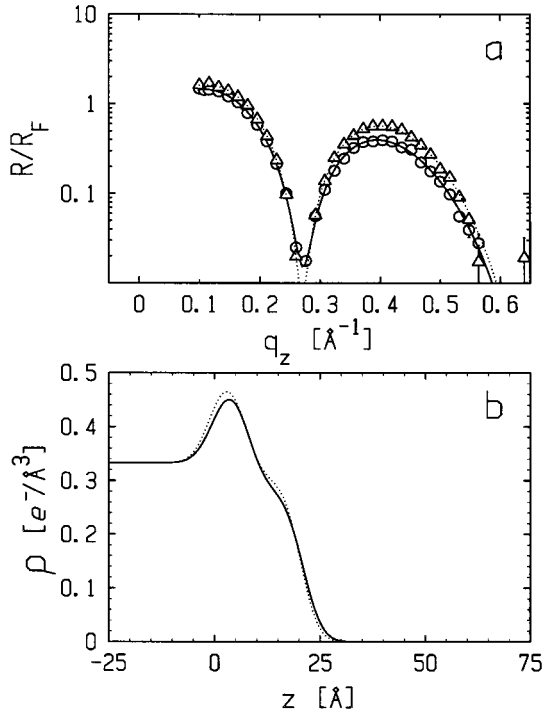

Figure 8. Normalized reflectivity data for pure DLPE monolayers as a function of applied surface pressure, π, on semilog (a) and linear (b) axes: $\pi = 37$ mN/m (solid, ○); $\pi = 42$ mN/m (dotted, △). (c) shows the electron density profile structures corresponding to these fits, constructed from the fit parameters appearing in Table 3.

α-helices of the lipopeptide relative to the air/water interface (Figure 7b). At the lowest pressures above the plateau (32 and 42 mN/m), the resulting electron density profile structures contain a prominent, electron dense feature at the junction between the two slabs (Figure 7b, solid and dashed curves). Comparing these profile structures with those obtained from pure DLPE monolayers (Figure 8b), we conclude that this feature must correspond to the headgroups of the lipid. The profiles terminate in a broad air/monolayer interface corresponding to the poorly ordered alkyl chains of the free phospholipid and the covalently bound palmitoyl chains of the lipopeptide.

Inspection of the electron density profile structures of the BBC16/DLPE monolayers (Figure 7b) shows that the

Table 3. Parameters Corresponding to the Fitted Reflectivity Curves Shown in Figure 8 for Pure DLPE Monolayers[a]

π (mN/m)	L_1 (Å)	ρ_1 (e^-/Å^3)	L_2 (Å)	ρ_2 (e^-/Å^3)	σ (Å)
37	7.7	0.507	13.2	0.281	3.6
42	8.2	0.506	13.2	0.300	3.3

[a] Two-slab fits with one overall roughness parameter.

applied surface pressure affects the phospholipid and peptide components of the monolayer differently. The phospholipid headgroup feature has maximal density near π_c and becomes broader and less dense as pressure increases. Ultimately, the headgroups become indistinguishable from the peptide density. The peptide region, on the other hand, grows steadily denser and thicker. Note though, that although the headgroup region is subsumed within the peptide region, the peptide density never exceeds that of the headgroup feature near π_c. Thus the peptide moieties' ordering improves while that of the headgroups declines.

One might expect that if the headgroups become indistinguishable from the peptide region, the data could be fit using a one-slab model, as proved adequate for the pure lipopeptide monolayers. However, two-slab models also provided the best fits for the higher pressure monolayers (π = 46, 51 mN/m). In these cases, though, the thinner slab no longer gives rise to the electron density peak of the PE headgroups and the decaying density of the hydrocarbon tails. Instead, it changes the shape of the hydrocarbon/air interface subtly by providing additional density for the hydrocarbon tails out at large z. The change is more pronounced when one considers the slab models with the interfacial roughnesses neglected (Figure 7c). Thus as the headgroup feature wanes, the length and density of the hydrocarbon tails increase, but their final values are still small compared with what is observed for pure DLPE. However, considering the excess area available to each chain due to the incomplete occupation of the area directly over the α-helices (as indicated by the isotherm, Figures 4 and 5d), this is to be expected. This excess area may also provide the headgroups the space to come out of register with each other vertically, especially since some DLPE molecules must be directly over the subphase while some must be over α-helices and interacting with the loop region of the peptide. In this way, the density of the headgroups becomes unobservable in the electron density profile structure at the highest pressures investigated.

Off-Specular Inplane Scattering. At pressures above π_c, monolayers of DLPE produce a single, readily observable GID peak at a d spacing of about 4.3 Å (Figure 9). At a pressure of 42 mN/m, the q_z-resolved Bragg rod scan of this peak showed the hydrocarbon chains to be untilted, as determined by calculations that model the hydrocarbon chains as cylindrical rods.[12,15] Integrated and q_z-resolved scans of the GID pattern produced by a 2:1 DLPE/BBC16 monolayer at this same pressure gave practically identical results, albeit with a weaker signal. However, a GID signal could not be found reliably for these mixtures. We first observed GID at 42 mN/m and saw it again at 50 mN/m, but not at pressures in between. The half-widths of the Lorentzian reflections seen for all the pure phospholipid and the phospholipid/lipopeptide mixture were about the same within the uncertainty in the fit (≈0.03°), implying exponentially decaying correlations extending over about 500 Å. It seems improbable that correlations could exist over such a long distance in the mixture of palmitoyl and lauroyl chains, which both the isotherms and the reflectivity data show contain a good deal of excess area, and that the tilt angle should be so small a value in both systems. More likely, the mixture is too disordered to produce GID, and the signal that we see actually comes from small domains of DLPE that did not mix with the lipopeptide but that are too small to affect the reflectivity substantially. This would explain the absence of a GID signal from the mixed monolayers at high pressures, since we would observe GID only in the case that the X-ray footprint on the sample contained one or more such domains.

We also sought a GID signal arising from the packing of the α-helices of the lipopeptide. We summed together consecutive, identical scans of the region of the total scattering angle $-10° < 2\theta_{xy} < -6°$, corresponding to the range of d spacings between about 9 and 15 Å. Keeping in mind that the cross-sectional area of an α-helix is about 5 times that of a single hydrocarbon chain and that the magnitude of the GID signal should scale as the number of scatterers squared ($I \propto N^2$), we collected data in this region roughly 25 times as long as we had in the region

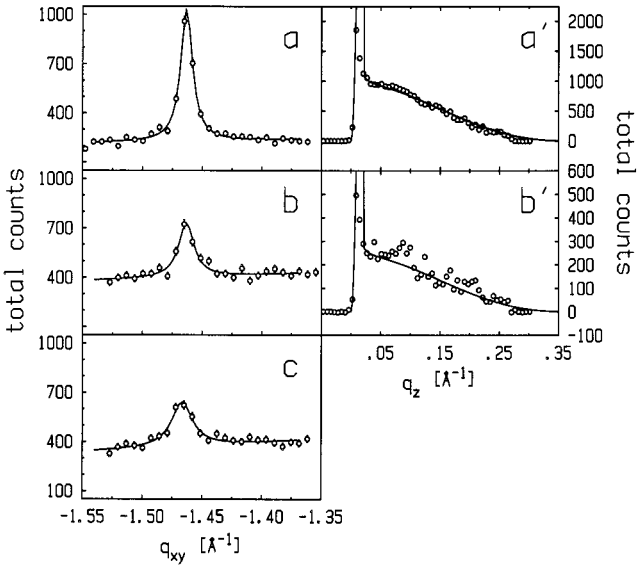

Figure 9. GID scans and the Lorentzian curves fit to the data (parameters given in Table 4): (a) pure DLPE, π = 42 mN/m; (b) 2:1 DLPE/BBC16 mixture, π = 42 mN/m; (c) 2:1 DLPE/BBC16 mixture, π = 50 mN/m. The primed figures show the data from q_z-resolved Bragg rod scans of GID peaks in the corresponding unprimed figures after background subtraction and the Bragg rod calculated when the alkyl chains of DLPE are modeled as cylinders with tilt = 0° (solid curve). q_z-resolved data were not collected for case (c). All data were collected with a position sensitive detector.

Table 4. Pure DLPE Monolayers and 2:1 DLPE/BBC16 Mixed Monolayers[a]

π (mN/m)	mean (Å^{-1})	d spacing (Å)	half-width (deg)
32[b]	−1.455	4.318	0.22
37[b]	−1.469	4.277	0.25
42[b]	−1.463	4.295	0.18
42[c]	−1.463	4.295	0.22
50[c]	−1.467	4.283	0.31

[a] Fit parameters from Lorentzian curves fit to GID peaks and associated physical quantities. [b] Pure DLPE monolayers. [c] 2:1 DLPE/BBC16 mixed monolayers.

(15) Als-Nielsen, J.; Kjaer, K. X-ray Reflectivity and Diffraction Studies of Liquid Surfaces and Surfactant Monolayers. In *Proceedings of a NATO Advanced Study Institute on Phase Transitions in Soft Condensed Matter Systems, Geilo, Norway, 4−14 April, 1989*; Riste, T., Sherrington, D., Eds.; Plenum Publishing Corp.: New York, 1989; Vol. 211.

corresponding to the hydrocarbon chain separation. But despite integrating for 100 min of data collection time, we were unable to detect any peak in the GID scan. (At the end of these scans, the GID peak due to the alkyl chains was still present and unchanged, indicating that the monolayer had withstood the radiation dose.) The data did not appear any different from that collected on a pure water subphase without a monolayer for a similar time period. After several attempts with different monolayers at surface pressures between 42 and 50 mN/m, we concluded that the absence of a GID signal meant that the α-helices did not form a two-dimensional crystal in the monolayer. We subsequently tried a different approach to inplane scattering that could detect order within the plane of the monolayer that was less than crystalline.

As we expected the scattering signal that might arise from a noncrystalline arrangement of the peptide to be very weak, we chose to work away from the equator ($q_z = 0$ Å^{-1}), to avoid the background that can be strong in this region, especially when the incident angle is below the critical angle.[16] We positioned the scintillation counter so that, in the plane of the reflection, the angle of inclination equaled the angle of declination ($\alpha = \beta = 0.9°$), with the vertical aperture before the detector set 11.5 mm high. At our sample-to-detector length of 600 mm, this permitted us to accept X-rays from a range of angles of inclination from the sample, $0.35° < \beta < 1.45°$, and thereby integrate over the range of momentum transfer, $0.05 < q_z < 0.2$ Å^{-1} (for this measurement, $\lambda = 1.546\ 83$ Å). This range was chosen to include the first maximum in the reflectivity of DLPE and the first two maxima of the mixed DLPE/BBC16 monolayer (Figures 6 and 8). Holding α and β fixed, we moved the detector out of the plane of the reflection and collected off-specular data as a function of the horizontal angle ($2\theta_{xy}$) between the detector and the direct beam. The data presented in Figure 10a are the average of four or five scans, each lasting about 1 h.

Since the peptide is embedded in the phospholipid matrix, we subtracted the normalized scattering data for the pure DLPE monolayer from the data for the mixed DLPE/BBC16 monolayer in order to isolate the signal due to the peptide. The resulting difference signal appears as a broad peak, which is approximately Gaussian, centered on $q_{xy} = 0.28$ Å^{-1} ($2\pi/22$ Å), with a standard deviation $\sigma = 0.143$ Å^{-1}. The monolayer should be cylindrically symmetric, with no preferred azimuthal direction, so the proper interpretation of this scattering signal, I_0, requires the computation of the radial autocorrelation function by means of an inverse Fourier−Bessel transform:[17]

$$A_0(r) = \int I_0(Q) J_0(2\pi Q r) 2\pi Q \, dQ \qquad (1)$$

where r and Q (=$(2/\lambda)$ sin $\theta_{xy} = q_{xy}/2\pi$) are the radial coordinates in real and reciprocal space, respectively, and J_0 is the zeroth-order Bessel function. The resulting autocorrelation function (Figure 11) has its first maximum at 17 Å, a distance somewhat smaller than the center of the untransformed data because the Bessel function enhances the weighting of the low-q data relative to the high-q data. This length corresponds to the distance of closest approach between nearest neighbors. The nearest-neighbor separation indicates that the peptide exists in a state of amorphously arranged dihelices, as consideration of the peptide's design and solution structure show. This distance cannot accommodate two four-helix bundles, which require a separation of at least 20 Å. Dihelices, on the other hand, may be separated by 10−20 Å, depending on the geometry of the packing arrangement, so we expect the average separation as determined by the experiment to lie between these two values. The observed separation of 17 Å lies close to the upper end of this range, which is consistent with the solution NMR structure of apo-BB.[18,19]

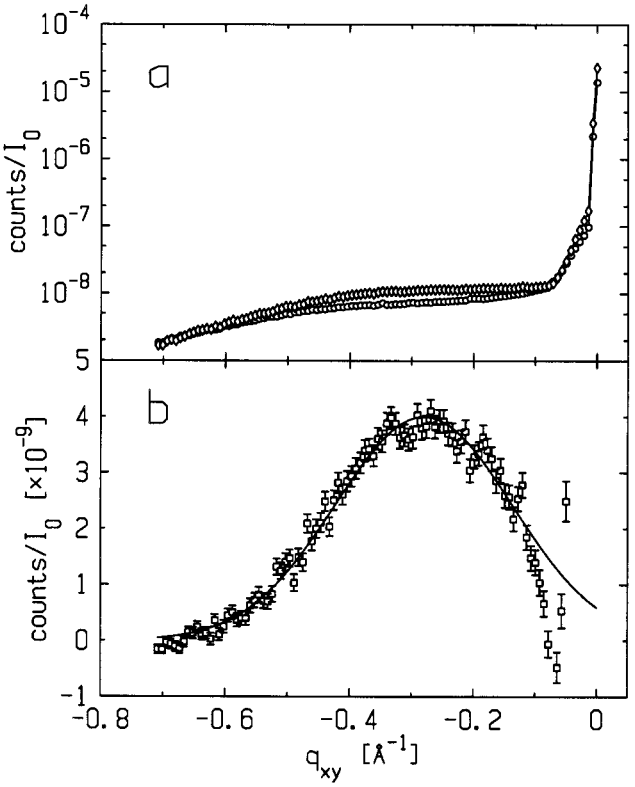

Figure 10. (a) Off-specular in-plane scattering data collected from a pure DLPE monolayer at $\pi = 28.6 \pm 0.2$ mN/m (○) and a mixed monolayer of DLPE and BBC16 in a ratio of 4:1 at $\pi = 30.5 \pm 0.5$ mN/m (◇), normalized by the monitor counts. (b) The difference between the two datasets displayed in part a. Note that the ordinate is now linear. The Gaussian curve (solid line) is merely intended to guide the eye and has a mean value $q_{xy} = -0.28$ Å^{-1} and standard deviation $\sigma = 0.143$ Å^{-1}.

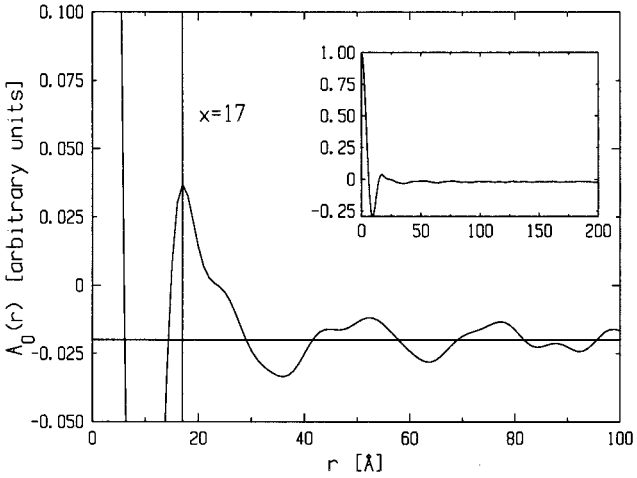

Figure 11. The radial autocorrelation function, computed via the inverse Fourier−Bessel transform of the difference signal presented in Figure 10b, exhibits a peak at $r = 17$ Å, yielding the distance of closest approach between neighboring molecules. The inset displays the entire range of the function computed.

(16) Blasie, J. K.; Fischetti, R. F. Unpublished data.
(17) Kataoka, M.; Ueki, T. *Acta Crystallogr.* **1980**, *A36*, 282−287.
(18) Gibney, B. R.; Rabanal, F.; Skalicky, J. J.; Wand, A. J.; Dutton, P. L. *J. Am. Chem. Soc.* **1999**, *121*, 4952−4960.

To gain some idea of the ability of these molecules to pack at the air/water interface, we computed the two-dimensional radius of gyration[20] from the atomic coordinates of the family of NMR structures and found that it ranged between 6.7 and 7.1 Å, a bit less than half of the nearest-neighbor separation obtained from the radial autocorrelation function and, therefore, in good agreement with this measurement.

Discussion. The various data from the different characterization methods that we applied to the mixed monolayers of BBC16 and DLPE provide a consistent and thorough picture of the structure of this system. The phospholipid and the lipopeptide mix only when constrained to do so by a deposition procedure that produces some initial surface pressure before compression begins, and then only partially. Some of the DLPE occupies excess area over the α-helices, and some of it competes with the lipopeptide for area at the air/subphase interface. As pressure is applied, the α-helices of the lipopeptide reorient in the same manner as was seen for pure BBC16. At pressures just above this orientational transition, and just above the fluid-to-gel transition of DLPE, reflectivity shows an electron-rich headgroup feature that penetrates the α-helices, as we expect from the isotherm data. Accordingly, the density of this feature is intermediate between that of the peptide moiety and that of the headgroups in a pure DLPE monolayer. Because so much of the phospholipid competes with the peptide for interfacial area, it does not enhance the ordering of the alkyl chains. In fact, the profile structure shows lower density for the hydrocarbon chains of the mixture than for the pure peptide monolayer. Consistent with this decrease in the density of the alkyl chains, we were unable to detect GID from the chains until we applied higher surface pressures. As pressure increases, the density of the peptide moiety grows, approaching the value of a well-packed protein film. At the same time, the density of the headgroup feature decreases and becomes indistinguishable from the peptide moiety. Apparently the excess area in among the mixed hydrocarbon chains allows enough freedom for the ethanolamine headgroups to disorder to the extent that their density (smeared along z) is the same as that of the peptide, and so they "vanish" from the profile structure of the monolayer. The chains themselves remain poorly ordered. Their density never attains as high a density as the chains of pure DLPE and tends to fall off monotonically without forming a shoulder. GID from the hydrocarbon chains becomes observable above 40 mN/m, but the dependence of its features on the applied surface pressure indicates that it must be due to phase-separated domains within the monolayer. The GID peak at 42 mN/m is broader than that in pure DLPE, indicating a shorter correlation length, and the ratio of the counts in the peak to the background level is only about 1:1, compared to 4:1 for DLPE. As pressure increases, the GID peak broadens and the amplitude decreases relative to the background. In pure DLPE and DMPE, the opposite trends occur. The observed trends would be consistent with phase-separated DLPE domains becoming increasingly perturbed by the surrounding DLPE/BBC16 mixed phase as pressure increases.

Additionally, it may be noted (data not shown) that 3:1 mixed monolayers of DLPE/BBC16 exhibit the orientational transition described for pure BBC16 and 2:1 DLPE/BBC16 mixtures, but 4:1 DLPE/BBC16 monolayers do not. These results are consistent with the conclusions above regarding the area mismatch between the hydrocarbon chain and α-helix cross sections and indicate that lateral compression of the peptide/water part of the monolayer is necessary to induce the orientational transition of the helices.

Crystalline domains of the α-helices of the peptide do not form in the mixed monolayers, and the off-specular scattering signal obtained from the difference between in-plane scattering scans of the mixed monolayer and pure DLPE shows that the monolayer consists of a two-dimensional liquid (or glass) of dihelical units. Most likely, this is also the state of the peptide within pure lipopeptide monolayers and within mixed monolayers with palmitic acid, as well, and accounts for the lack of a GID signal in our earlier investigations of these systems.

Indirect evidence from NMR measurements and spectroscopic measurements on peptides labeled with chromophores indicate that BB forms an anti-four-helix bundle, with the α-helices of each dihelix antiparallel. In a series of peptides with related primary sequences, the ones that formed syn-four-helix bundles, with the α-helices of each dihelix parallel, gave broad NMR spectra with poor dispersion, indicating that these peptides did not adopt a largely unique conformation the way naturally occurring proteins do. Anti-four-helix bundles, on the other hand, gave spectra with good dispersion from which high-resolution structural information could be obtained. This probably contributes to the lack of GID from the α-helices and also points out a peculiar feature of monolayer construction at interfaces. The asymmetric nature of the interface forces the peptide to orient vectorially at high pressure, with the palmitoyl chains in contact with the gaseous phase. Thus the dihelices are all in a syn configuration with respect to each other; i.e., all the α-helices are parallel. As this is apparently the less structurally defined configuration of the BB four-helix bundle, vectorial orientation of the peptide may have prevented formation of more rigid four-helix bundles and 2-D crystallization of the monolayer. The anti configuration might be achieved in a suitably annealed Langmuir monolayer consisting of a 50:50 mixture of dihelices alkylated at their amino termini and dihelices alkylated at their carboxy termini.

Conclusions

These experiments demonstrate our ability to create designed, vectorially oriented peptide monolayers at the air/water interface and emphasize the overriding importance of the asymmetric interface in the design process. H10H24, the archetypical bundle of two amphipathic, dihelical units, associated only weakly with the interface, as it was designed with only solution properties in mind. As a result, the monolayers were unstable at high pressure and we could only observe the peptide as dihelical units lying in the plane of the interface. The palmitoylated derivative BBC16 associated with the interface more strongly and formed monolayers sufficiently stable for us to observe the transition in the orientation of the peptide that occurs at high pressures ($\geq$30 mN/m), when the α-helices of the peptide become nearly perpendicular to the interface. The most stable monolayers consist of BBC16 associated with a matrix of DLPE. We conducted a detailed study of the profile and in-plane structures of monolayers composed of 2:1 DLPE/BBC16 mixtures.

The present work has already influenced two other areas of investigation. First, the work conducted at the air/water interface provides insight to help guide investigation of

(19) Skalicky, J. J.; Gibney, B. R.; Rabanal, F.; Urbauer, R. J. B.; Dutton, P. L.; Wand, A. J. *J. Am. Chem. Soc.* **1999**, *121*, 4941−4951.

(20) *Macromolecules 1*: *Structure and Properties*; Plenum Press: New York, 1977.

maquette peptide monolayers transferred to solid supports by Langmuir−Blodgett (LB) techniques. Care must be taken in applying conclusions drawn from Langmuir films to LB films, as it has been shown that the deposition process can change the structure of the film.[21,22] Indeed, maquette peptide LB monolayers in which the orientation of the α-helices normal to the interface apparently was not preserved upon transfer to solid supports have already been described.[3] However, under appropriate conditions, when the support is suitably "softened" by a self-assembled monolayer, the orientation can be maintained through the LB deposition process.[2] Deposited over electrodes, such films may allow a more complete realization of the potential of maquette peptides for studying the electron-transfer properties of proteins by facilitating correlated structural and electrochemical measurements. Second, the great stability of the DLPE/BBC16 mixed monolayers is sufficient for us to employ neutron reflectivity to study these monolayers. By replacing the amino acid at any selected site in the sequence of the 31-mer with a deuterated version of the same amino acid, we alter the neutron scattering properties of the peptide without altering its structure. Comparing the reflectivity from a series of different peptides H^2-labeled in this manner, we may extract a set of key distances which determine the internal structure of the peptide from neutron reflectivity measurements.[23] If sufficient resolution could be obtained, this technique could prove useful for studying structural perturbations caused by the binding of prosthetic groups to the peptide.

Acknowledgment. The authors wish to express their gratitude to Paul Heiney and David Gidalevitz for help with the early part of this work, to Elaine Dimasi for alignment of the spectrometer and helpful discussions, to Scott Coburn and John Gray for technical assistance, to Ann Edwards, Larry Kneller, Erik Nordgren, Andrey Tronin, and Songyan Zheng for helping collect the data, to Connie Blasie for implementing the box refinement algorithm in Mathematica, and to David Vaknin for the generously allowing us to use his trough. This work supported by the NIH under Grants GM33525 and GM41048 and by the MRSEC Program of the NSF under Award Number DMR96-32598.

Appendix. The Box-Refinement Algorithm

Box refinement provides an iterative, model-independent method of obtaining the phase of (and thereby recovering the electron density distribution that gave rise to) the scattered intensity collected in a reflectivity experiment.[24,25] Our group has used it successfully to solve the electron density profile structure of a variety of lipid and protein thin films on solid supports.[26−28] To apply this method, two criteria must be met. First, the structure must be of finite extent in one direction. This is as true of Langmuir films in the direction normal to the monolayer/air interface as it is for the films on solid supports to which we have already applied the algorithm. Second, the data being analyzed must be from the kinematical limit in which the incident beam is scattered weakly, with only a single scattering event for each photon in the scattered beam. In this limit, the scattering potential and the scattering amplitude are Fourier transform pairs (the first Born approximation). In the usual reflectivity formalism,[9,10] the normalized reflectivity is obtained from the observed reflectivity R by dividing out the Fresnel function[29] R_F: $|\Phi(q)|^2 = R/R_F$. This quantity is related to the electron density distribution of the sample $\rho(z)$ as follows

$$F(q_z') = \frac{1}{\rho_\infty} \int \left\langle \frac{d\rho}{dz} \right\rangle e^{iq_z'z}\, dz \qquad (2)$$

where ρ_∞ is the electron density of the semi-infinite slab underlying the monolayer and the transformation $q_z'^2 = q_z^2 - q_c^2$ improves the rigorousness of the equation as $q \rightarrow q_c$ by applying a correction to the momentum transfer, which occurs within the monolayer.[30] In other words, the second condition is met by the normalized reflectivity and the *derivative* of the electron density distribution. Since the derivative of the electron density profile structure is also finite in extent, we can apply the box-refinement algorithm to the normalized reflectivity data in order to recover the derivative and integrate it to obtain the electron density distribution of the sample. If the profile structures so obtained agree with those computed from the parameters of slab models fit to the data, they provide an independent check on the convergence of the fit to the global best fit and on the appropriateness of the model used. The examples shown here represent the first application of the box-refinement algorithm to normalized reflectivity data.

The box-refinement algorithm provides a method for transforming an initial arbitrary trial structure into a structure that correctly predicts the experimentally observed intensity function. The heart of the algorithm is the box constraint: the correct solution will be finite in extent and of the same size as the actual structure. This

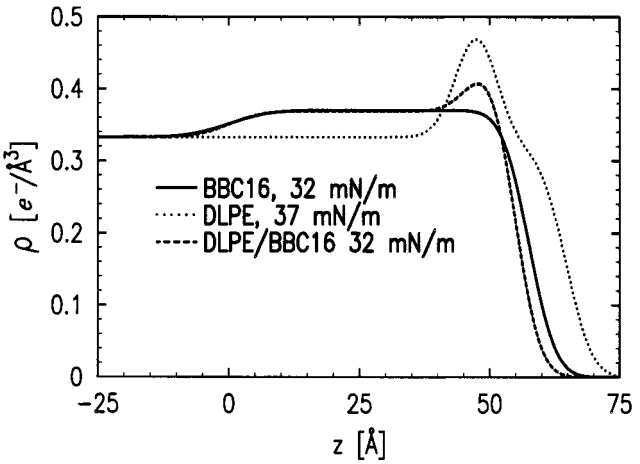

Figure 12. Superposition of the profile structures obtained for DLPE-containing monolayers: pure BBC16 at $\pi = 33$ mN/m (solid curve), pure DLPE at $\pi = 37$ mN/m (dotted), and 2:1 DLPE/BBC16 mixture at $\pi = 32$ mN/m (dashed). The profiles shown are the same as in Figures 3b and 8b (solid curve) and 7b (solid curve), respectively.

(21) Riegler, J. E.; LeGrange, J. D. *Phys. Rev. Lett.* **1988**, *21*, 2492−2495.
(22) LeGrange, J. D. *Phys. Rev. Lett.* **1991**, *66*, 37−40.
(23) Blasie, J. K.; Timmins, P. *MRS Bull.* **1999**, 40−47.
(24) Stroud, R. M.; Agard, D. A. *Biophys. J.* **1979**, *25*, 495−512.
(25) Makowski, L. *J. Appl. Crystallogr.* **1981**, *14*, 160−168.
(26) Fischetti, R. F.; Filipkowski, M.; Garito, A. F.; Blasie, J. K.; *Phys. Rev. B* **1988**, *37*, 4714−4726.
(27) Pachence, J. M.; Blasie, J. K. *Biophys. J.* **1991**, *59*, 894−900.
(28) Skita, V.; Filipkowski, M.; Garito, A. F.; Blasie, J. K. *Phys. Rev. B* **1986**, *34*, 5826−5837.

(29) The Fresnel function describes the reflectivity from an abrupt interface between two media, and is given by $R_F(q) = |(q - (q^2 - q_c^2)^{1/2})/(q + (q^2 - q_c^2)^{1/2})|^2$, where the critical q-vector for total external reflection is $q_c = (4\pi/\lambda)\sin(\lambda(\rho r_0/\pi)^{1/2})$ with λ the X-ray wavelength and r_0 (=2.82 × 10^{-5} Å) the scattering length of an electron.
(30) Lösche, M.; Piepenstock, M.; Diedereich, A.; Grünwald, T.; Kjaer, K.; Vaknin, D. *Biophys. J.* **1993**, *65*, 2160−2177.

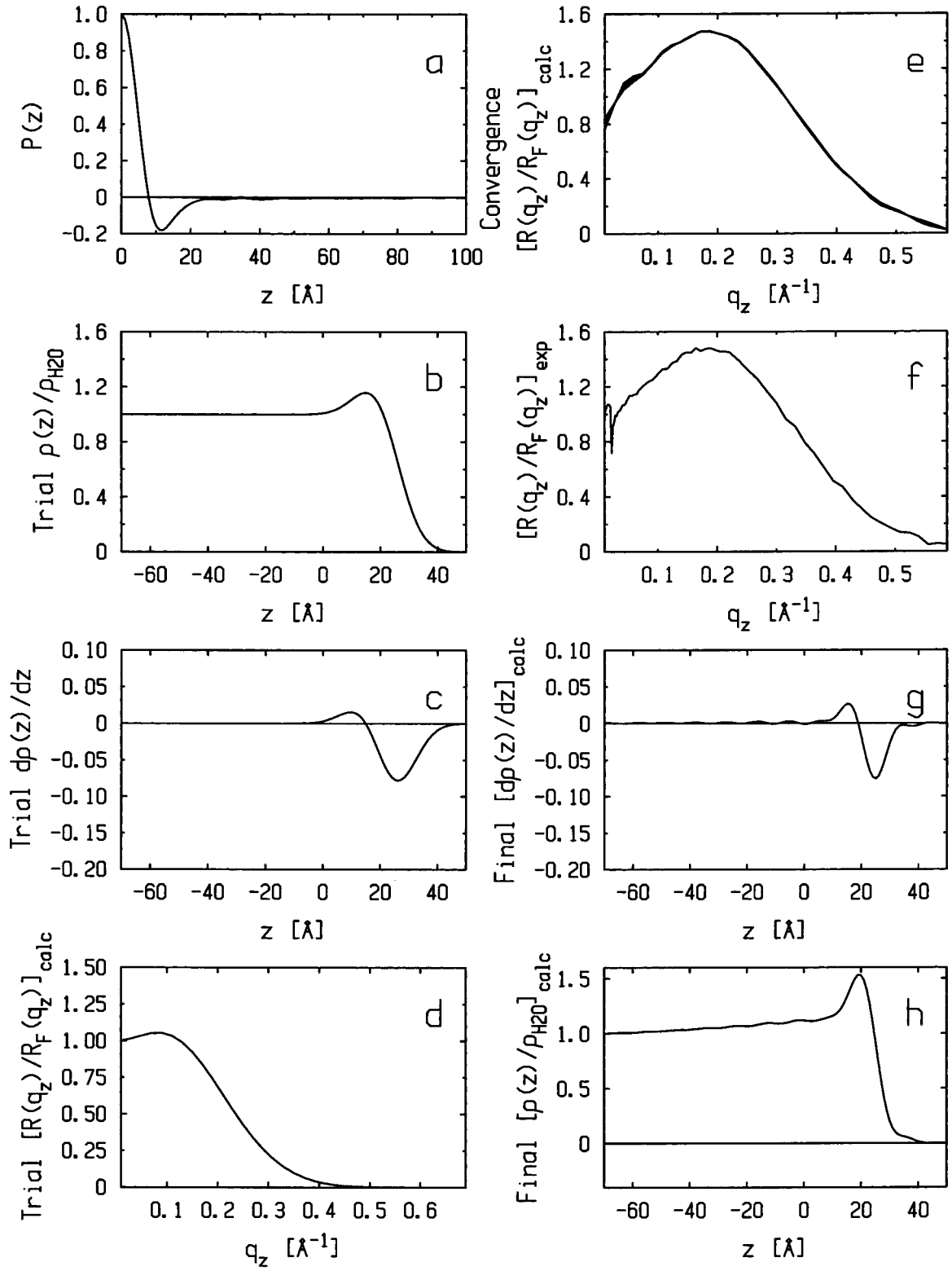

Figure 13. See Appendix for details.

size can be obtained from the experimental data without any assumptions by computing its inverse Fourier transform. This operation yields the autocorrelation function of the derivative of the electron density distribution (the Patterson function). If the monolayer has a thickness L, the significant oscillations in the Patterson function will die out beyond $\pm L$, as correlations cannot extend over distances larger than the structure itself.

The estimated thickness of the monolayer, the box constraint, is first input to the algorithm. We also input the square root of the normalized reflectivity after transforming the independent coordinate to account for the medium (see comment after eq 2), $|\Phi_{exp}(q_z')|$, which gives the magnitude of the Fourier transform of the derivative of the electron density distribution $d\rho/dz$. We start the algorithm with an arbitrary trial structure, $(d\rho/dz)_0$ (a clearly incorrect choice works best), and compute its Fourier transform. We discard the magnitude of the Fourier transform but retain the resulting phase function, ϕ_1. We use ϕ_1 to compute the inverse Fourier transform

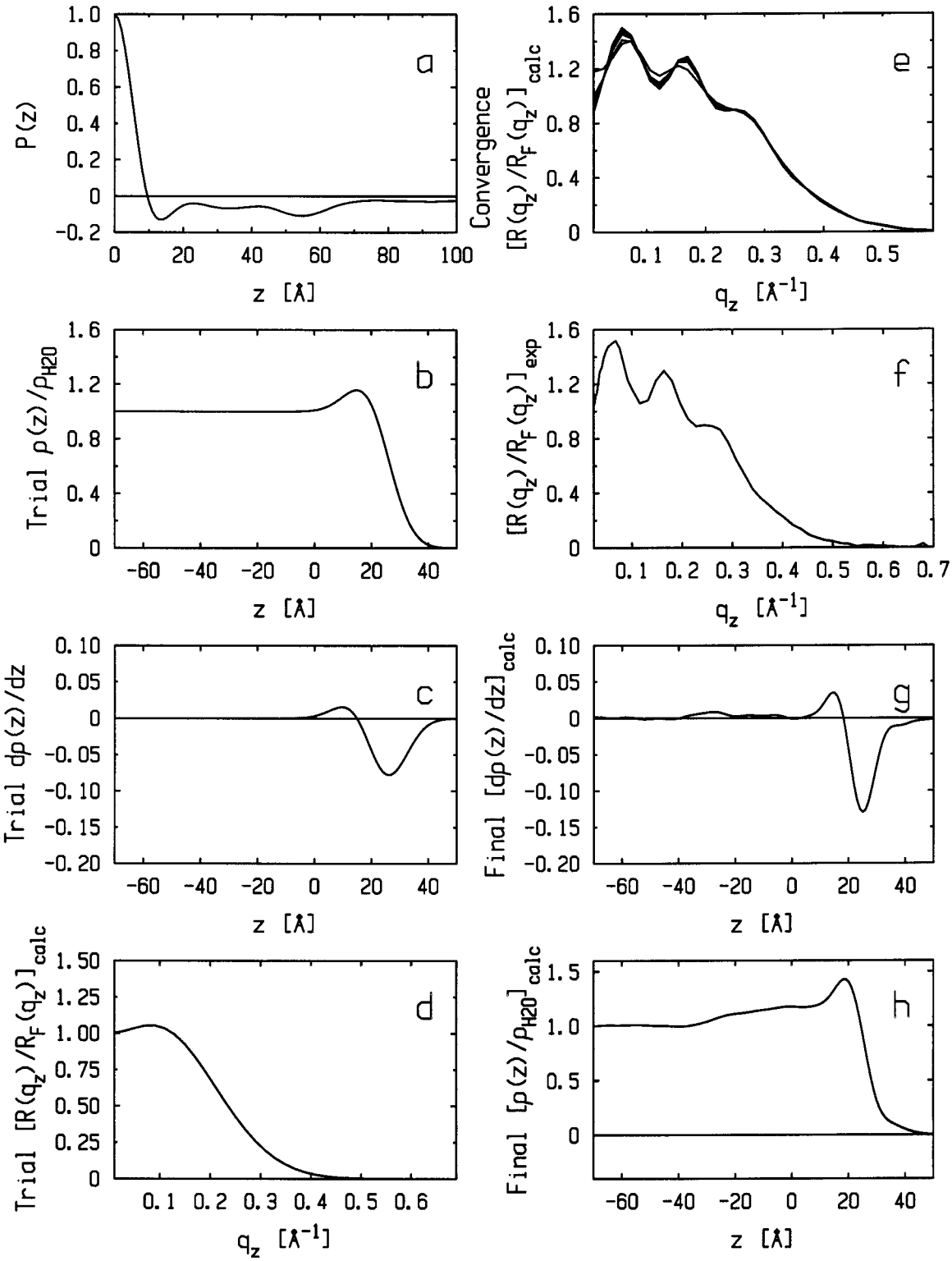

Figure 14. See Appendix for details.

of $|\Phi_{exp}(q_z')|$ and obtain a new structure, $(d\rho/dz)_1$. At this point, we apply the box constraint. The function $(d\rho/dz)_1$ is truncated to remove the portions beyond the limits $0 < z < L$ to obtain $(d\rho/dz)_{1t}$. Now we compute the Fourier transform of $(d\rho/dz)_{1t}$. We check the progress of the refinement by comparing the square of this Fourier transform with $|\Phi_{exp}(q_z')|^2$. If the agreement is poor (as is generally the case after the first iteration), we repeat the procedure with $(d\rho/dz)_{1t}$ as the input trial structure. We take the phase from its Fourier transform and compute the inverse Fourier transform of $|\Phi_{exp}(q_z')|$ to obtain $(d\rho/dz)_2$; we apply the box constraint to get $(d\rho/dz)_{2t}$; we compute the Fourier transform and compare its square to $|\Phi_{exp}(q_z')|^2$ to check the progress of the refinement; if necessary, $(d\rho/dz)_{2t}$ becomes the input trial structure for the next iteration, and so on. The algorithm converges when the agreement between $|\Phi_{exp}(q_z')|^2$ and the square of the Fourier transform of $(d\rho/dz)_n$ is good and there is little change between $(d\rho/dz)_n$ and $(d\rho/dz)_{n+1}$. The derivative can then be integrated to obtain the electron density

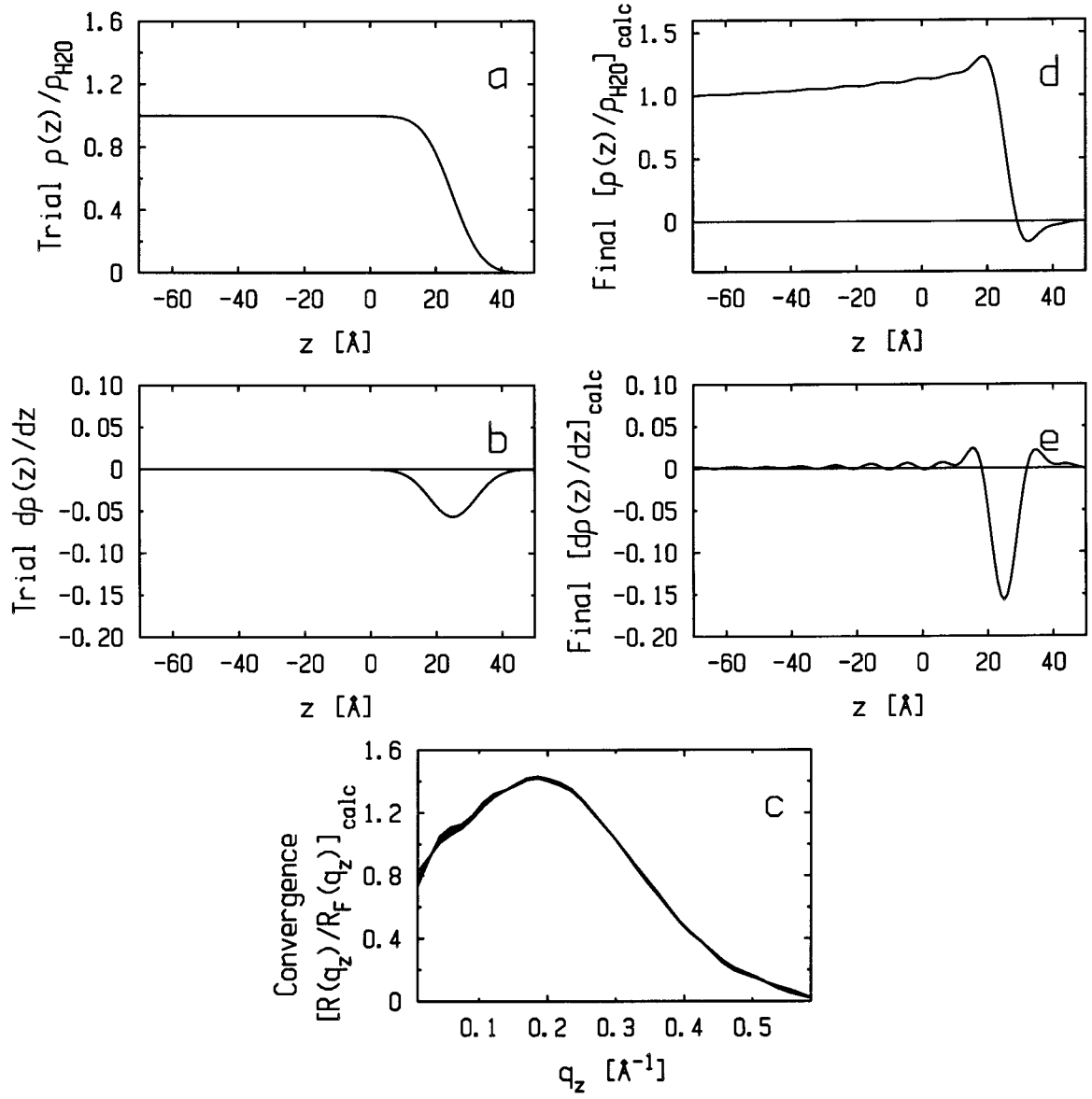

Figure 15. See Appendix for details.

distribution that produced the observed reflectivity. The constant of integration and scale of the distribution are recovered by imposing the conditions $\rho_{+\infty} = 0$ and $\rho_{-\infty} = 0.333$ e$^-$/Å^3.

By way of example, we apply the algorithm to data collected from 2:1 DLPE/BBC16 monolayers at 22 and 32 mN/m, that is, below and above the plateau in the isotherm, in Figures 13 and 14, respectively. As the peptide changes its orientation from parallel to the plane of the interface to normal to it, the autocorrelation function, computed via the inverse Fourier transform of the reduced reflectivity data, extends to larger z (panel a). For consistency, in both cases we use the same box constraint, the range shown in panel b, much bigger than the Patterson function indicates is necessary. We also use the same trial profile structure, a step preceded by a slight increase in density (shown in panel b on a scale normalized by the subphase density), even though the calculated reflectivity from this trial profile structure does not produce secondary maxima, as seen in the experimental data for the higher pressure case (compare panel d with panel f). Convergence of the algorithm is checked by observing the reflectivity calculated from the electron density distribution derivative, $d\rho/dz_n$, obtained after each iteration of the algorithm (panel e shows this for $n = 1$, 2, ..., 10, 20, 30, 40, 50) and comparing it to the experimental data (panel f). The final derivatives, $d\rho/dz_{50}$, appear in panel g. For the low-pressure case, this consists of a single peak and trough, along with some ripple due to the finite q-range of the data, while in the high-pressure case additional maxima appear to the left of the peak and trough at the edge of the derivative. After integration, the results are in good agreement with those obtained from fitting the data with slab models (compare Figure 13h with Figure 7a and Figure 14h with the solid curve in Figure 7b).

Figures 15 and 16 illustrate how the choice of the initial trial function affects the results obtained. The same low-pressure data for a 2:1 DLPE/BBC16 monolayer from Figure 13 are used in both Figures 15 and 16, but in Figure 15 the trial function is a simple step while in Figure 16 it is a step preceded by a slight decrease in density. The three cases, Figures 13b, 15b, and 16b, may be said to represent, respectively, trial functions biased toward, neutral to, and biased away from the actual electron density distribution that produced the experimentally

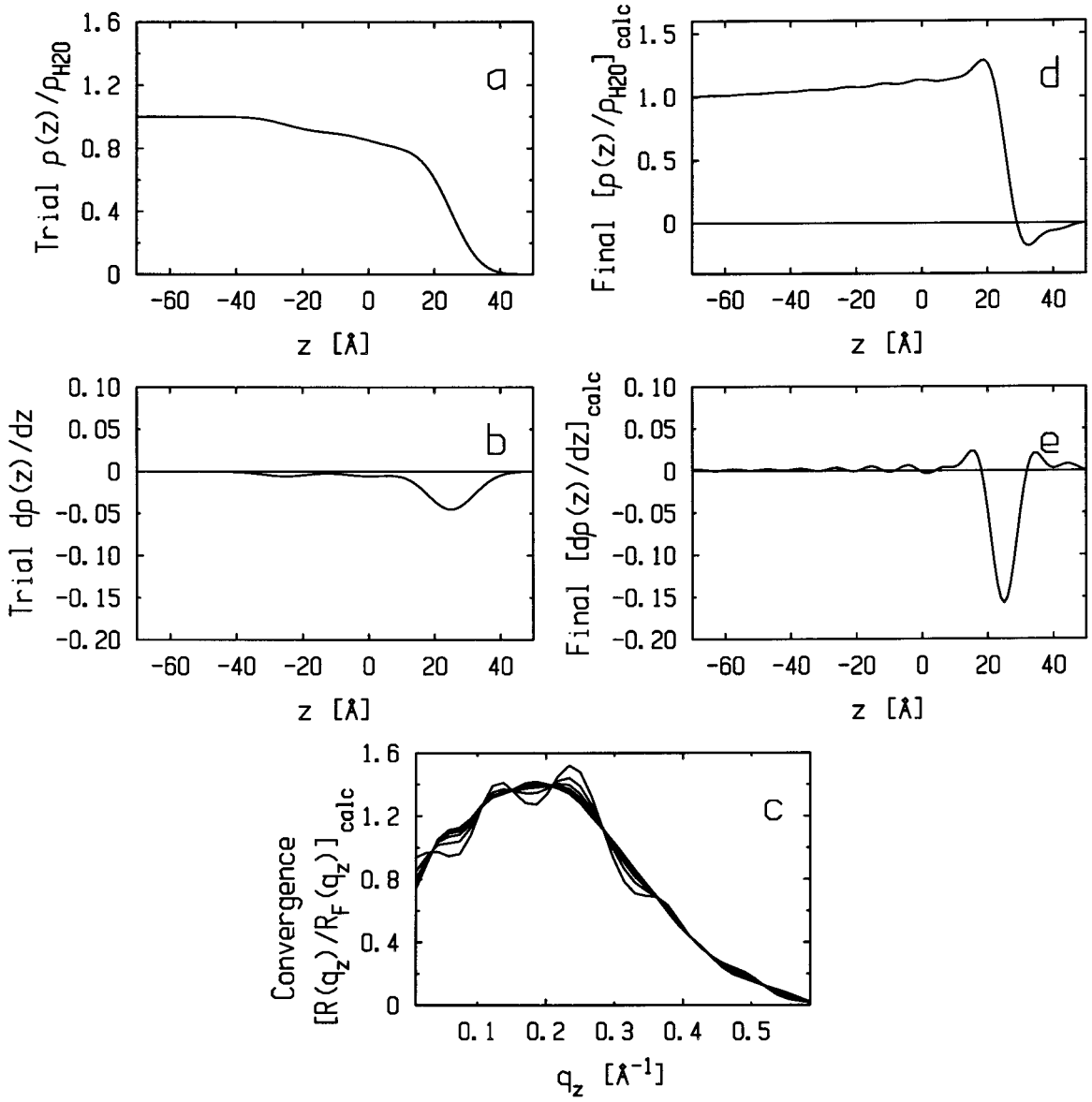

Figure 16. See Appendix for details.

observed reflectivity. As may be expected, for the trial structure with its density enhanced before the step, the trial structure that resembles the final result most closely, the algorithm converges the most rapidly, as demonstrated in superposition of the reflectivity calculated from iterations 1, 2, ..., 10, 20, 30, 40, 50 (Figure 13e). It converges almost as quickly for the neutral trial function of the simple step, but it converges significantly more slowly for the trial function with the depression before the step, as can be seen in panel c, which shows the superposition of the reflectivity calculated from the same iterations as in the other figures. Remarkably, in all cases, the algorithm recovers the same final electron density derivatives and distributions (compare panels g and h in Figure 13 with panels d and e in Figures 15 and 16).

LA000264Z